Metastructure With Piezoelectric Element for Simultaneous Vibration Suppression and Energy Harvesting

Guobiao Hu
Department of Mechanical Engineering,
University of Auckland,
Auckland 1010, New Zealand

Lihua Tang[1]
Department of Mechanical Engineering,
University of Auckland,
Auckland 1010, New Zealand
e-mail: l.tang@auckland.ac.nz

Arnab Banerjee
Department of Mechanical Engineering,
University of Auckland,
Auckland 1010, New Zealand

Raj Das
Department of Mechanical Engineering,
University of Auckland,
Auckland 1010, New Zealand;
Sir Lawrence Wackett Aerospace Research Centre,
School of Engineering,
RMIT University,
Melbourne 3001, Australia

Inspired by the mechanism of acoustic–elastic metamaterial (AEMM) that exhibits a stop band gap for wave transmission, simultaneous vibration suppression and energy harvesting can be achieved by integrating AEMM with energy-harvesting component. This article presents an analytical study of a multifunctional system based on this concept. First, a mathematical model of a unit-cell AEMM embedded with a piezoelectric transducer is developed and analyzed. The most important finding is the double-valley phenomenon that can intensively widen the band gap under strong electromechanical coupling condition. Based on the mathematical model, a dimensionless parametric study is conducted to investigate how to tune the system to enhance its vibration suppression ability. Subsequently, a multicell system is conceptualized from the findings of the unit-cell system. In a similar way, dimensionless parametric studies are conducted to optimize the vibration suppression performance and the energy-harvesting performance severally. It turns out that different impedance matching schemes are required to achieve optimal vibration suppression and energy harvesting. To handle this problem, compromising solutions are proposed for weakly and strongly coupled systems, respectively. Finally, the characteristics of the AEMM-based piezoelectric energy harvester (PEH) from two functional aspects are summarized, providing several design guidelines in terms of system parameter tuning. It is concluded that certain tradeoff is required in the process of optimizing the performance toward dual functionalities. [DOI: 10.1115/1.4034770]

1 Introduction

Metamaterials are artificial materials with unique properties, such as negative refraction [1,2], negative modulus [3,4], and negative effective density [5,6], derived from intentionally designed internal microstructures. One of the most attractive features of the metamaterials is the ability to restrict the wave transmission over a specified frequency range, which is termed as band gap. Band gap control and tailoring becomes one of the most popular research interests in the field of metamaterials. Applications of metamaterials include vibration suppression [7], sound isolation [8], and acoustic waveguiding [9]. To achieve vibration suppression in a broad frequency range, Huang and Sun [10] proposed and studied a multiresonator acoustic metamaterial which can exhibit multiple band gaps. Based on this idea, Tan et al. [11] optimized the band gap of a dual-resonator acoustic metamaterial and demonstrated that its band gap could be much wider than that of the conventional single-resonator design. The proposed dual-resonator metamaterial is able to suppress the vibration more effectively in a wider frequency range. Other attempts to widen the band gap by tuning system parameters have been reported in Refs. [7,12]. A theoretical study of band gap control through introducing negative capacitance piezoelectric shunting has been reported by Chen et al. [13]. In their mathematical model, the negative capacitance shunted piezoelectric element that has a negative capacitance ratio dependent stiffness was used as the spring to connect the main mass and the local resonator. Therefore, the band gap of the metamaterial could be controlled by tuning the negative capacitance ratio. To sum up, numerous researches have been conducted regarding the band gap issue for better use of metamaterials for vibration suppression.

In recent years, the applications of metamaterials have been extended into the field of energy harvesting [14]. Inspired from the structure of Bragg scattering based phononic crystal, Carrara et al. [15] introduced three concepts: wave focusing, energy localization, and wave guiding. Correspondingly, they designed an acoustic mirror, an imperfect two-dimensional lattice system, and an acoustic funnel to enhance the energy-harvesting performance of the energy harvester placed inside these structures. Based on the mechanism of AEMM that is often referred to as locally resonant phononic crystal by some researchers, Shen et al. [16] designed a phononic crystal plate with an array of spiral beams as conversion medium for energy harvesting and reported that the output power was enhanced at a dozen of resonant frequencies within a low-frequency range. Mikoshiba et al. [17] proposed an energy-harvesting system with periodic structure embedded with multiple local resonators made of spring-suspended magnets. The oscillations of the magnets induced the current in the coils fixed outside. They claimed that their energy harvester possessed the functionality of vibration suppression as well, but they only investigated the energy-harvesting performance in their experiment. In a recent research reported by Ahmed et al. [18], they designed and experimentally tested a unit-cell AEMM-based energy harvester. Though their system intrinsically owned the functionality of vibration suppression derived from the properties of AEMM, they did not analyze and evaluate the system in terms of this functionality.

Based on the review of recent state-of-the-art literature, it can be seen that though a few researchers have attempted to employ acoustic–elastic metamaterials for energy harvesting, the research in this area is still in its infancy stage. The existing literature concentrated on the energy-harvesting performance utilizing the properties of metamaterials. The variations in the metamaterials properties in terms of the stop band gap accompanied with the energy harvesting are yet to be investigated. A few questions arising from here include: How can we achieve optimal energy-harvesting performance and vibration suppression? Is the

[1]Corresponding author.

Contributed by the Technical Committee on Vibration and Sound of ASME for publication in the Journal of Vibration and Acoustics. Manuscript received March 23, 2016; final manuscript received August 31, 2016; published online November 23, 2016. Assoc. Editor: Michael Leamy.

harvested power optimal at the local resonant frequency? and Does the optimal power correspond to the optimal vibration suppression? This paper is motivated to answer these questions.

In this paper, the performance of AEMM-based PEH with dual functionalities is investigated and discussed through analytical studies. First, the mathematical model of a unit-cell AEMM system embedded with a piezoelectric transducer is developed. Based on the mathematical model, a dimensionless parametric study is conducted to investigate how the band gap pattern, i.e., the vibration suppression performance, of the system is affected with varying parameters. The double-valley phenomenon is observed in the piezoelectric-coupled AEMM, which can intensively enhance the band gap effect. Subsequently, a multicell system is conceptualized from the findings of the unit-cell system. Investigations on both the vibration suppression performance and the energy-harvesting performance are conducted. Finally, in the attempt to optimize the performance of the system toward dual functionalities, different impedance matching schemes and different parameter tuning strategies are developed. Compromising solutions and design guidelines are provided to deal with these conflicts.

2 Unit-Cell System

2.1 Mathematical Model of Unit-Cell System. In the studies of metamaterials, a basic unit-cell model of AEMM is always referred to as a spring–mass system [5,11] or mass-in-mass system [6,19], which can be mathematically modeled as an outer sphere having mass m_1 connected with an inner ball of mass m_2 suspended by a spring with a constant k_2. The spring connecting the outer sphere to the base has a constant k_1. The AEMM is engineered so that it can exhibit transmission stop band gap for incident acoustic–elastic waves for vibration suppression. Obviously, AEMM has the applications where environmental vibrations exist. Fortuitously, this provides an opportunity to employ AEMM as a ready medium to impart the system an auxiliary function, i.e., energy harvesting by inserting a piezoelectric transducer. A conceptual schematic is shown in Fig. 1.

The governing equations of this model can be written as

$$m_2\ddot{u}_2 + c_2(\dot{u}_2 - \dot{u}_1) + k_2(u_2 - u_1) + \theta v = 0 \tag{1}$$

$$m_1\ddot{u}_1 + c_1(\dot{u}_1 - \dot{u}_0) + k_1(u_1 - u_0) + c_2(\dot{u}_1 - \dot{u}_2) + k_2(u_1 - u_2) - \theta v = 0 \tag{2}$$

$$\frac{v}{R} + C^S\dot{v} - \theta(\dot{u}_2 - \dot{u}_1) = 0 \tag{3}$$

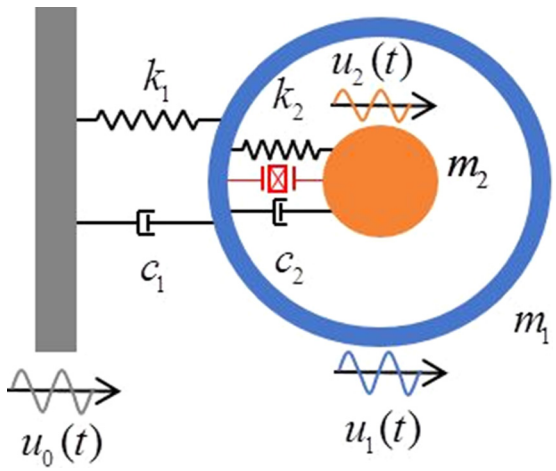

Fig. 1 Unit-cell AEMM-based PEH

where u_0, u_1, and u_2 are the absolute displacements of the base, outer mass , and inner mass , respectively; c_1 and c_2 are the damping coefficients of the outer mass and inner mass , respectively; θ is the electromechanical coupling coefficient; C^S is the clamped capacitance of the piezoelectric transducer; R is the electric resistor connected to the piezoelectric transducer; and v is the voltage across R. Applying the Laplace transform and setting the Laplace operator $s = j\omega$ (ω is the circular excitation frequency), we obtain

$$-(k_2 + j\omega c_2)U_1 + (k_2 - m_2\omega^2 + j\omega c_2)U_2 + \theta V = 0 \tag{4}$$

$$(k_1 + k_2 - m_1\omega^2 + j\omega c_1 + j\omega c_2)U_1 - (k_2 + j\omega c_2)U_2 - \theta V = (k_1 + j\omega c_1)U_0 \tag{5}$$

$$j\omega\theta U_1 - j\omega\theta U_2 + (1/R + j\omega C^S)V = 0 \tag{6}$$

where U_i ($i = 1,2$) and V denote the amplitudes of u_i ($i = 1,2$) and v, respectively. Solving Eqs. (4)–(6) simultaneously, we have the transmittance of the system τ [20]

$$\tau = \frac{U_1}{U_0} = \frac{\alpha^2 + j2\alpha\zeta_1\Omega}{\alpha^2 - (1+\mu)\Omega^2 + j2\alpha\zeta_1\Omega - \dfrac{\mu\Omega^4}{1 - \Omega^2 + j2\zeta_2\Omega + \dfrac{jrk_e^2\Omega}{1 + jr\Omega}}} \tag{7}$$

The dimensionless voltage can be derived as

$$\left|\frac{V}{\dfrac{m_2\omega^2U_0}{\theta}}\right| = \left|\frac{\dfrac{jrk_e^2\Omega}{1+jr\Omega}\cdot\dfrac{\alpha^2+j2\alpha\zeta_1\Omega}{\alpha^2-(1+\mu)\Omega^2+j2\alpha\zeta_1\Omega}}{1-\Omega^2+j2\zeta_2\Omega-\dfrac{\mu\Omega^4}{\alpha^2-(1+\mu)\Omega^2+j2\alpha\zeta_1\Omega}+\dfrac{jrk_e^2\Omega}{1+jr\Omega}}\right| \tag{8}$$

and the dimensionless power as

$$\left|\frac{P}{\dfrac{m_2(\omega^2U_0)^2}{\omega_2}}\right| = \frac{rk_e^2\Omega^2}{1+(r\Omega)^2}\left|\frac{\dfrac{\alpha^2+j2\alpha\zeta_1\Omega}{\alpha^2-(1+\mu)\Omega^2+j2\alpha\zeta_1\Omega}}{1-\Omega^2+j2\zeta_2\Omega-\dfrac{\mu\Omega^4}{\alpha^2-(1+\mu)\Omega^2+j2\alpha\zeta_1\Omega}+\dfrac{jrk_e^2\Omega}{1+jr\Omega}}\right|^2 \tag{9}$$

in which, the dimensionless parameters are

$$\alpha = \frac{\omega_1}{\omega_2} = \frac{\sqrt{k_1/m_1}}{\sqrt{k_2/m_2}};\quad \zeta_1 = \frac{c_1}{2\sqrt{k_1m_1}};\quad \zeta_2 = \frac{c_2}{2\sqrt{k_2m_2}};\quad \mu = \frac{m_2}{m_1};$$
$$r = \omega_2C^SR;\quad k_e^2 = \frac{\theta^2}{C^Sk_2};\quad \Omega = \frac{\omega}{\omega_2}$$

The energy-harvesting performance of a two degrees-of-freedom piezoelectric system shown in Fig. 1 has been discussed in Tang and Yang [21]. Hence, Sec. 2.2 focuses on the vibration suppression of the unit-cell system in the presence of piezoelectric coupling.

2.2 Investigation on Vibration Suppression Performance. The performance of attenuating the vibration is quantitatively described by system transmittance τ. The plot of the transmittance

τ versus the normalized circular frequency Ω is used to evaluate the vibration suppression performance of the system over a spectrum. Due to the presence of local resonance, there exists a band gap in the transmittance of AEMM, which, by definition in the metamaterial context, is the frequency range within which $\tau < 1$ or $\tau\,(\mathrm{dB}) < 0$. The term "band gap pattern" used hereafter refers to the features of band gaps, which determine the vibration suppression performance of AEMM.

2.2.1 Effects of k_e on Vibration Suppression Performance. From Eq. (3), it is noted that if $R \to 0$, i.e., short-circuit condition, the voltage v approaches zero and thus the last term on the left-hand side in both Eqs. (1) and (2) disappears. In other words, the voltage v does not affect the equations of motion. On the other hand, if $R \to +\infty$, i.e., open circuit condition, the first term in Eq. (3) becomes negligible, then we can find that $\dot{v}$ is proportional to the relative velocity $(\dot{u}_1 - \dot{u}_0)$. By integrating both sides, we can conclude that v is proportional to the relative displacement $(u_1 - u_0)$. By substituting the voltage in Eq. (1), we find that the coupling effect acts as additional stiffness of θ^2/C^S between the inner and the outer masses. For an intermediate condition (with an electrical load of finite value R), we can speculate that the coupling effect will result in a combination of additional stiffness and damping on the mechanical structure. The effective stiffness k_2' and damping c_2' due to electromechanical coupling are varied with different electrical loads. Incorporate the effect of electromechanical coupling into k_2' and c_2' and express Eq. (4) in terms of k_2' and c_2' as

$$-(k_2' + j\omega c_2')U_1 + (k_2' - m_2\omega^2 + j\omega c_2')U_2 = -m_2\omega^2 U_2 + (k_2' + j\omega c_2')(U_2 - U_1) = 0 \tag{10}$$

On the other hand, substituting Eq. (6) into Eq. (4) to eliminate V, we yield

$$-m_2\omega^2 U_2 + \left(k_2 + j\omega c_2 + \frac{j\omega\theta^2}{(1/R + j\omega C^S)}\right)(U_2 - U_1) = 0 \tag{11}$$

Comparing Eqs. (10) and (11), we can obtain k_2' and c_2' as

$$k_2' = k_2 + \frac{C^S R^2\omega^2\theta^2}{1 + (R\omega C^S)^2} \tag{12}$$

$$c_2' = c_2 + \frac{R\theta^2}{1 + (R\omega C^S)^2} \tag{13}$$

We then define the ratio of k_2'/k_2 and c_2'/c_2, which can be derived as

$$\left(\frac{k_2'}{k_2}\right) = 1 + \frac{r^2 k_e^2\Omega^2}{1 + (r\Omega)^2} \tag{14}$$

$$\left(\frac{c_2'}{c_2}\right) = 1 + \frac{r k_e^2}{2\zeta_2\left(1 + (r\Omega)^2\right)} \tag{15}$$

For a given $\mu = 0.2$, $\alpha = 0.9$, $\zeta_1 = 0.02$, $\zeta_2 = 0.004$, and $k_e = 0.8$, Fig. 2(*a*) depicts how these two ratios are affected by r.

With the increase of r, c_2'/c_2 first increases drastically then decreases, while k_2'/k_2 increases constantly. The lower bound of k_2'/k_2 is one, which means that there is no additional stiffness at short-circuit condition, and the upper bound is $1 + k_e^2$ (find the limit of Eq. (14) as r approaches positive infinite). This provides a possibility to alter the local resonance frequency of the system through r. Stimulated by this idea, we select r to tune the local resonance frequency to adapt to each excitation frequency to maximally attenuate vibrations. Similar to the impedance matching technology used to achieve maximal power output [22], by sweeping r at each frequency, the band gap pattern comprising optimal transmittance is shown in Fig. 2(*b*). It is noted that there appears a double-valley phenomenon, one valley is fixed in the vicinity of the local resonance frequency $\omega = \omega_2 = \sqrt{k_2/m_2}$, $\Omega = 1$, while the other is movable and centered around $\Omega = \sqrt{1 + k_e^2}$, corresponding to the maximal effective local resonance frequency due to an electromechanical coupling under open circuit condition $\omega = \omega_2' = \sqrt{1 + k_e^2} \cdot \omega_2$. Apart from the appearance of the double-valley phenomenon, it is also noted that with the increase of k_e, magnitudes of both peaks in the band gap pattern decrease, and the decreasing trend of the magnitude of the second peak is more evident. Based on the above results, it can be inferred that embedding a piezoelectric transducer and introducing a stronger electromechanical coupling can be utilized to improve the vibration suppression ability of AEMM.

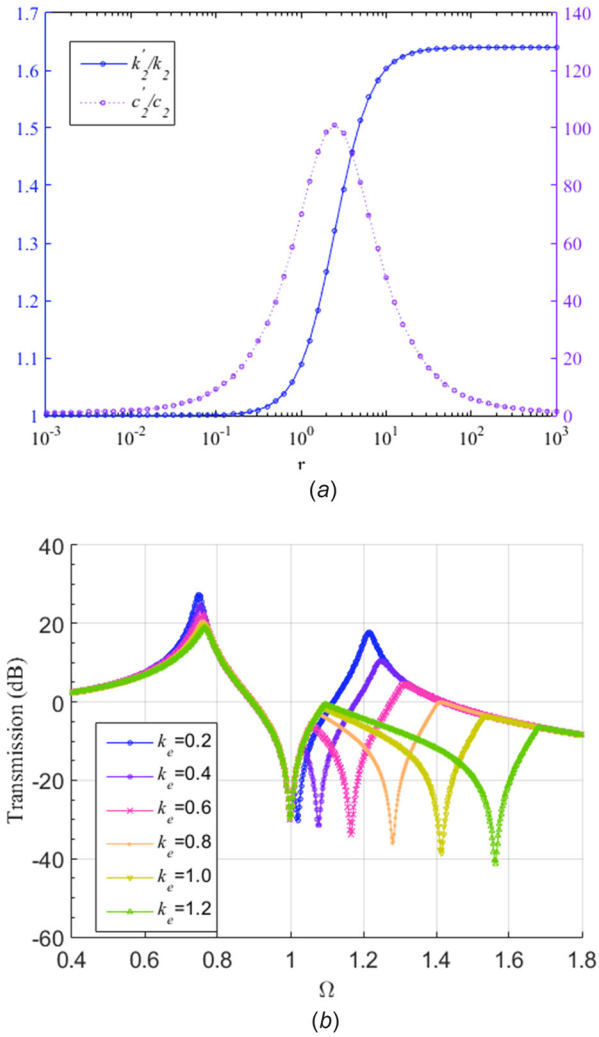

Fig. 2 (*a*) k_2'/k_2 and c_2'/c_2 versus r and (*b*) optimal transmittance (impedance matching is achieved at each frequency) versus Ω for different k_e

From Fig. 2(*b*), the double-valley phenomenon becomes evident when the coupling is strong. Hence, we are especially interested in investigating the vibration suppression for a strongly coupled system. For the following case studies, unless we explicitly state that one or several of them are varying, it is assumed that the dimensionless system parameters are $\mu = 0.2$, $\alpha = 0.9$, $\zeta_1 = 0.02$, $\zeta_2 = 0.004$, and $k_e = 0.4$. And, r is always swept to achieve minimal transmittance at each frequency.

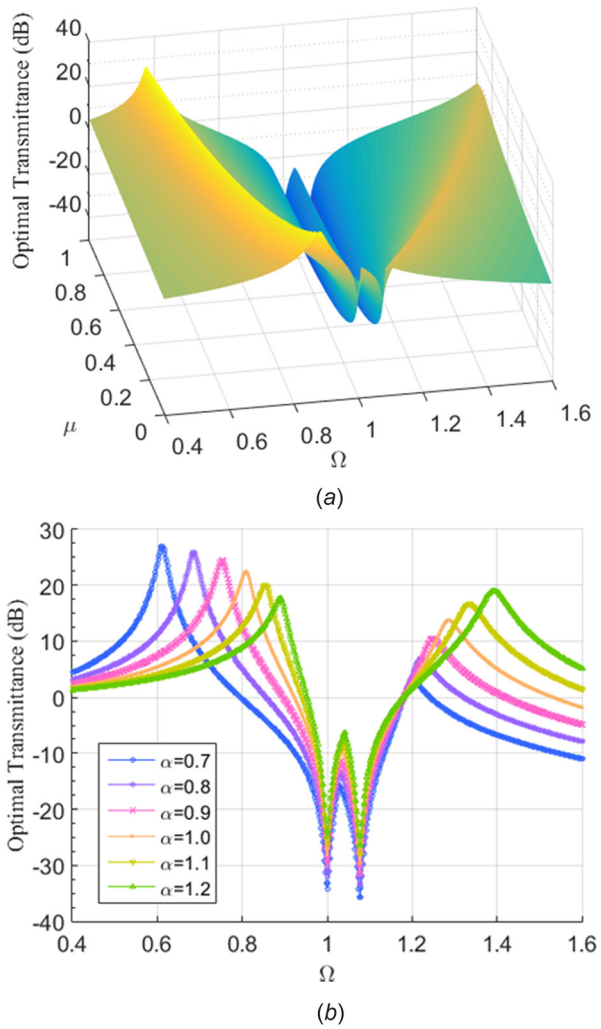

Fig. 3 (*a*) Optimal transmittance versus μ and Ω and (*b*) optimal transmittance versus Ω for different α

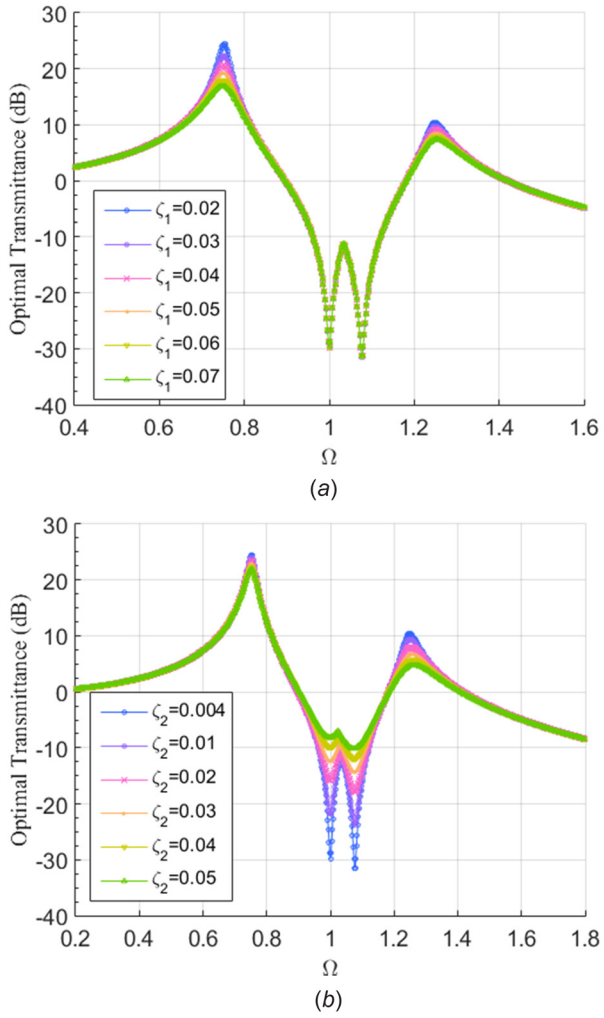

Fig. 4 Optimal transmittance versus Ω for (*a*) different ζ_1 ($\zeta_2 = 0.004$) and (*b*) different ζ_2 ($\zeta_1 = 0.02$)

2.2.2 Effects of μ on Vibration Suppression Performance. The band gap characteristic of AEMM is due to the local resonance of the additional attached inner mass with out-of-phase motion when the external excitation frequency is near the local resonance frequency. It can be speculated that the heavier the inner mass, the more evident the "band gap" effect. In contrast, if the inner mass is too light (the extreme case is to exclude the inner mass), its out-of-phase motion will have such a minor effect on the dynamics of the outer mass that the band gap effect disappears. Hence, it is worth investigating the effect of mass ratio μ on the band gap pattern.

With fixed α, ζ_1, and ζ_2, by varying the mass ratio μ and the excitation angular frequency Ω, the transmittance τ versus μ and Ω is illustrated in Fig. 3(*a*). It is noted that the aforementioned double-valley phenomenon appears. The first valley corresponds to the intrinsic local resonance of the inner mass, while the second valley is formed due to the strong electromechanical coupling effect which significantly alters the effective stiffness of the inner system and hence its local resonance frequency. Besides, with the increase of μ, it is observed that: the band gap becomes wider; the magnitude of the first peak initially decreases quickly then increases slowly; and the magnitude of the second peak constantly decreases and both valleys become deeper. Hence, from the vibration suppression perspective, a larger μ (i.e., a heavier inner mass) is preferred to achieve a wider gap and deeper valleys.

2.2.3 Effects of α on Vibration Suppression Performance. Apart from the mass ratio μ, the inner spring stiffness k_2 can affect the band gap pattern as well. Assume that the inner spring is extremely hard (i.e., the inner and outer masses are linked by a rigid bar), the local resonance frequency will be extremely high and meaningless and can be regarded as disappeared. Figure 3(*b*) shows how the band gap pattern is affected by α. With the increase of α, the magnitude of the second peak increases, while the magnitude of the first peak decreases. This provides a possibility to tune the magnitudes of peaks, which may be useful for vibration control in different situations. For example, in the case that the excitation frequency is known in the high-frequency range (i.e., $\Omega > 1$), decreasing α can suppress the second peak for vibration control purpose. In contrast, increasing α is recommended to suppress the first peak for the case of low-frequency excitation (i.e., $\Omega < 1$). In addition, a smaller α is always preferred in terms of the wider and deeper band gap.

2.2.4 Effects of ζ on Vibration Suppression Performance. In the area of metamaterials, little attention has been paid to the effect of the damping on the band gap pattern. Damping is excluded from the models in the reported literature [10,19]. Based on the knowledge of mechanical vibrations, it is intuitive to infer that the increase of damping can flatten the peaks. Figures 4(*a*) and 4(*b*) depict the effects of ζ_1 and ζ_2 on the band gap pattern, respectively, to verify our speculations. From Fig. 4(*a*) ($\zeta_2 = 0.004$), it is noted that the first peak dominates the vibration suppression behavior. With the increase of ζ_1, the magnitudes of both peaks decrease, and the magnitude of the first peak is more sensitive to ζ_1. From Fig. 4(*b*) ($\zeta_1 = 0.02$), it is noted that with the increase of ζ_2, the magnitudes of both peaks also decrease.

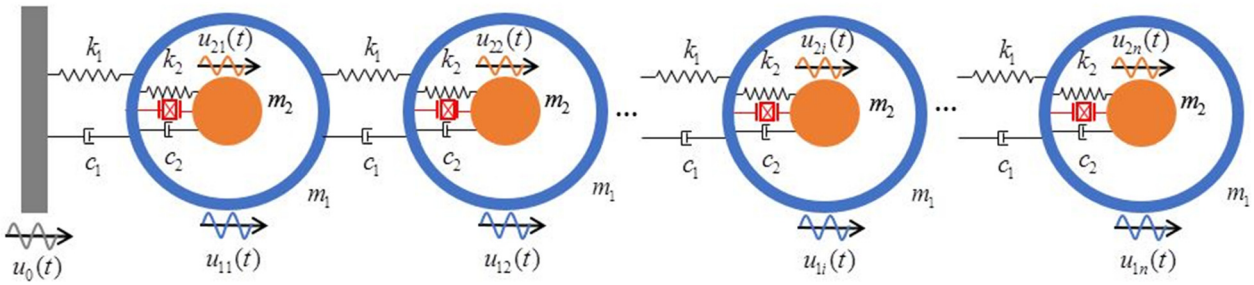

Fig. 5 Multicell AEMM-based PEH

The magnitude of the second peak is more sensitive to ζ_2 but it is not dominant to the overall vibration suppression performance. Moreover, the valleys become shallower with the increase of ζ_2. Overall, a larger ζ_1 and meanwhile a smaller ζ_2 are recommended to improve the vibration suppression performance of the system.

3 Multicell System

From this section, the unit-cell model will be extended to the multicell model, and the wave transmission properties along with the energy-harvesting performance will be investigated in the presence of piezoelectric coupling.

3.1 Mathematical Model of Multicell System. It can be expected that more peaks in the frequency responses can be achieved due to more degrees-of-freedom in the system, which can help widen the bandwidth of energy harvesting. Mikoshiba et al. [17] experimentally studied the energy-harvesting performance of a multicell system based on electromagnetic transduction, but the influence of electromechanical coupling on the functionality of vibration suppression of AEMM was not considered. In this section, both aspects will be investigated.

As shown in Fig. 5, for a multicell system, each unit is inserted with a piezoelectric transducer. For the sake of simplicity, we assume that all the unit cells have the same system parameters: m_1, m_2, k_1, k_2, c_1, and c_2, and all the transducers have the same C^S and θ. Each transducer is connected with a resistor R with the same value. Based on this simplification, the governing equations of this model are written as

$$\begin{cases} m_2\ddot{u}_{2i} + c_2(\dot{u}_{2i} - \dot{u}_{1i}) + k_2(u_{2i} - u_{1i}) + \theta v_i = 0 \\ m_1\ddot{u}_{1i} + c_1(2\dot{u}_{1i} - \dot{u}_{1(i+1)} - \dot{u}_{1(i-1)}) + c_2(\dot{u}_{1i} - \dot{u}_{2i}) + k_1(2u_{1i} - u_{1(i+1)} - u_{1(i-1)}) + k_2(u_{1i} - u_{2i}) - \theta v_i = 0 \\ m_1\ddot{u}_{1n} + c_1(\dot{u}_{1n} - \dot{u}_{1(n-1)}) + c_2(\dot{u}_{1n} - \dot{u}_{2n}) + k_1(u_{1n} - u_{1(n-1)}) + k_2(u_{1n} - u_{2n}) - \theta v_n = 0 \\ v_i/R + C^S\dot{v}_i - \theta(\dot{u}_{2i} - \dot{u}_{1i}) = 0 \end{cases} \tag{16}$$

For u_{1i} and u_{2i}, the second subscript stands for the ith unit-cell. Solving Eq. (16), we obtain

$$\begin{cases} U_{1(n-1)} = \dfrac{1}{\alpha^2 + j2\alpha\zeta_1\Omega}\left(\alpha^2 - \Omega^2 + j2\alpha\zeta_1\Omega - \mu\Omega^2\dfrac{1 + j2\zeta_2\Omega + \dfrac{jrk_e^2\Omega}{1+jr\Omega}}{1 - \Omega^2 + j2\zeta_2\Omega + \dfrac{jrk_e^2\Omega}{1+jr\Omega}}\right)U_{1n} \\ U_{1(i-1)} = \dfrac{1}{\alpha^2 + j2\alpha\zeta_1\Omega}\left(\alpha^2 - \Omega^2 + j2\alpha\zeta_1\Omega - \mu\Omega^2\dfrac{1 + j2\zeta_2\Omega + \dfrac{jrk_e^2\Omega}{1+jr\Omega}}{1 - \Omega^2 + j2\zeta_2\Omega + \dfrac{jrk_e^2\Omega}{1+jr\Omega}}\right)U_{1i} - U_{1(i+1)} \\ U_0 = \dfrac{1}{\alpha^2 + j2\alpha\zeta_1\Omega}\left(\alpha^2 - \Omega^2 + j2\alpha\zeta_1\Omega - \mu\Omega^2\dfrac{1 + j2\zeta_2\Omega + \dfrac{jrk_e^2\Omega}{1+jr\Omega}}{1 - \Omega^2 + j2\zeta_2\Omega + \dfrac{jrk_e^2\Omega}{1+jr\Omega}}\right)U_{11} - U_{12} \end{cases} \tag{17}$$

Through iterative substitution, we can represent the magnitudes of displacements of outer masses in each cell as

$$U_{1i} = B_i U_0 \tag{18}$$

The transmittance of the multicell system is defined as

$$\tau = \left|\frac{U_{1n}}{U_0}\right| = \left|B_n\right| \tag{19}$$

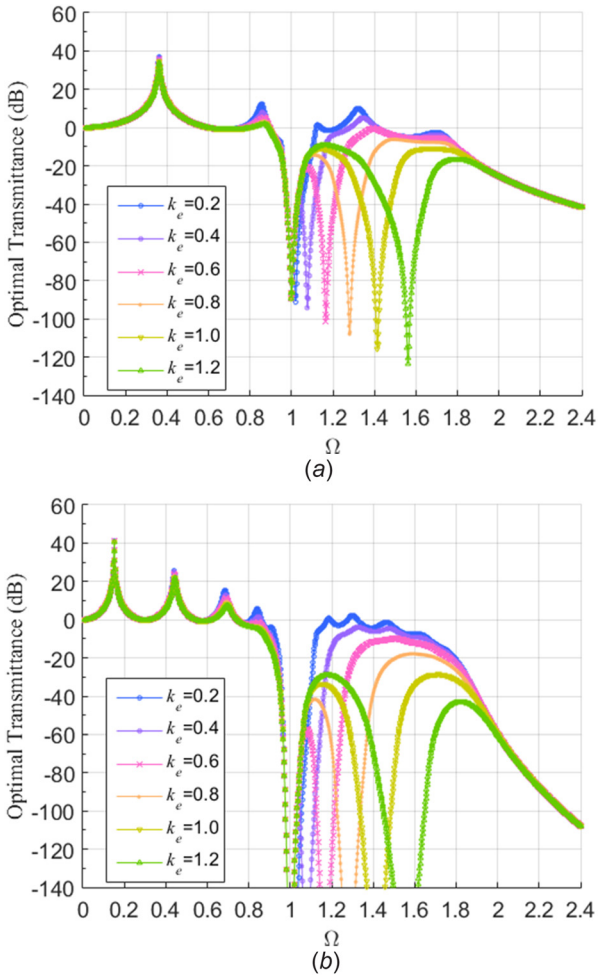

Fig. 6 Optimal transmittance versus Ω for different k_e : (*a*) $n = 3$ and (*b*) $n = 8$

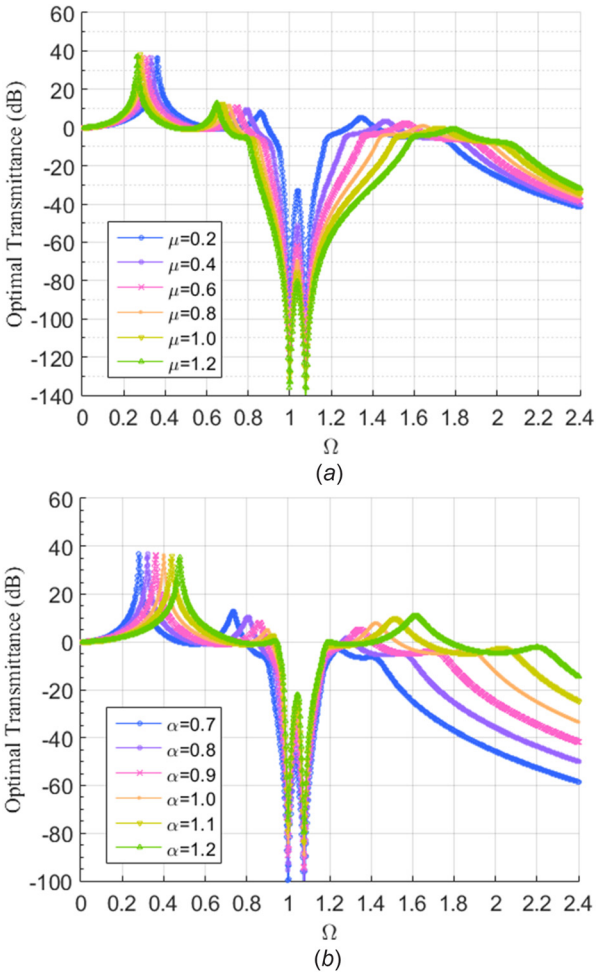

Fig. 7 Optimal transmittance versus Ω for (*a*) different μ and (*b*) different α

The dimensionless voltage across the resistor connected to the ith piezoelectric transducer is

$$\left|\frac{V_i}{\frac{m_2\omega^2 U_0}{\theta}}\right| = \left|\frac{B_i \cdot \frac{jrk_e^2\Omega}{1+jr\Omega}}{1-\Omega^2+j2\zeta_2\Omega+\frac{jrk_e^2\Omega}{1+jr\Omega}}\right| \tag{20}$$

And, the dimensionless power is

$$\left|\frac{P_i}{\frac{m_2(\omega^2 U_0)^2}{\omega_2}}\right| = r\left|\frac{B_i \cdot \frac{k_e\Omega}{1+r\Omega j}}{1-\Omega^2+j2\zeta_2\Omega+\frac{jrk_e^2\Omega}{1+jr\Omega}}\right|^2 \tag{21}$$

3.2 Investigation on Vibration Suppression Performance. Without loss of generality, we consider a multicell system composed of three unit cells.

3.2.1 Effects of k_e on Vibration Suppression Performance. Similar to the unit-cell system, the electromechanical coupling effect can influence the effective stiffness and the effective damping of the inner system in all the unit cells and thus the local resonant frequency. Based on the same mechanism, minimal transmittance can be achieved by tuning r at each frequency. An example with $n = 3; \mu = 0.2; \alpha = 0.9; \zeta_1 = 0.02;$ and $\zeta_2 = 0.004$ is given to demonstrate this. Figure 6(*a*) shows the band gap pattern variation with the increase of k_e. Though the band gap pattern becomes more complicated than that for a unit-cell system due to more peaks brought by the multiple degrees-of-freedom, we can find that the effect of k_e on the band gap pattern is similar to the unit-cell system—with the increase of k_e, the double-valley phenomenon becomes more evident and the magnitudes of peaks in the band gap pattern decrease. Besides, it is noted that the double-valley phenomenon affects the peaks near the band gap and peaks in the high-frequency range significantly. The left-hand side peaks near the band gap are significantly suppressed with the increase of k_e, while the first peak, which is relatively far away from the band gap, is insensitive to k_e. Those peaks in high frequencies on the right-hand side of the band gap even disappear for strong coupling, replaced by the second valley. This conclusion still holds even we increase the number of unit cells (Fig. 6(*b*)).

Knowing that the coupling effect on the band gap pattern is more evident with the increase of coupling, we assume $k_e = 0.4$ for the following case studies.

3.2.2 Effects of μ on Vibration Suppression Performance. Given $\alpha = 0.9; \zeta_1 = 0.02;$ and $\zeta_2 = 0.004$, Fig. 7(*a*) illustrates how the band gap pattern is affected by μ. We can find that the effect of μ on the width of the band gap of the multicell system is similar to the unit-cell system—with the increase of μ, the gap becomes wider. While, the effect of μ on the magnitudes of peaks is more complex for the multicell system. For the peaks in the low-frequency range, their magnitudes increase with the increase of μ. The peak nearer to the band gap is more sensitive to μ (i.e., a

more evident increase in the magnitude of the peak). However, it is totally different in the high-frequency range, the magnitudes of the peaks decrease with μ, and the peak farther away from the band gap has a more significantly suppressed amplitude. Hence, we can conclude that a larger μ can be selected to increase the width of the band gap and overall improve the vibration suppression performance of the system. This conclusion still holds if we increase the number of unit cells.

3.2.3 Effects of α on Vibration Suppression Performance. Similarly, the effect of α on the band gap pattern of the three-cell system is also concerned. Given $\mu = 0.2; \zeta_1 = 0.02;$ and $\zeta_2 = 0.004$, Fig. 7(*b*) illustrates how the band gap pattern is affected by α. First, it is noted that the influence of α on the band gap width and the valley depth is similar to the unit-cell system: with the increase of α, both the gap width and the valley depth decrease. Second, the shift of the peak location is more significant for the peaks on the right-hand side of the band gap compared to those on the left-hand side. Third, due to the existence of more peaks in the band gap pattern of a multicell system, the variation in the peak magnitudes becomes more complicated than that in a unit-cell system—magnitudes of peaks far away from the band gap especially for those on the left-hand side of the band gap are insensitive to α. With the increase of α, magnitudes of peaks at the left fringe of the band gap decrease dramatically, while magnitudes of peaks on the right side of the band gap increase. A common feature for peaks at both sides is that the nearer the peak is to the band gap, the more sensitive it is to α. In terms of the magnitudes of peaks, it is hard to say whether a larger or smaller α is better to enhance vibration suppression performance. However, in terms of the band gap width and depth, a smaller α is always a better option. These conclusions hold for all the n-cell systems though results are not presented here.

3.2.4 Effects of ζ on Vibration Suppression Performance. Other than μ and α, the effect of damping ratio is investigated. For fixed $\mu = 0.2; \alpha = 0.9;$ and $\zeta_2 = 0.004$, the effect of ζ_1 on the band gap pattern is revealed in Fig. 8(*a*). Similar to the unit-cell system, with the increase of ζ_1, the magnitudes of all the peaks decrease. Then, we increased the number of cells and repeated the above study, it is found that ζ_1 can have a global effect on the magnitudes of all the peaks and has minor effect on the band gap. In a similar way, the effect of ζ_2 is investigated. With $\mu = 0.2; \alpha = 0.9;$ and $\zeta_1 = 0.02$, Fig. 8(*b*) depicts the responses of the system with the varying ζ_2. In terms of the band gap pattern, we note that it is similar to that of the unit-cell system, i.e., the depth decreases substantially with the increase of ζ_2. In terms of the magnitudes of peaks, the first peak is insensitive to ζ_2, while the magnitudes of other peaks decrease with the increase of ζ_2. Again, with the increased number of cells, though the result is not presented here, we find that the magnitudes of peaks far away from the band gap are insensitive to ζ_2, especially those on the left-hand side of the band gap. While the magnitudes of the peaks near the band gap are sensitive to ζ_2 and decrease significantly with it. Based on the above results, for the sake of vibration suppression, one should select a larger ζ_1, while a smaller ζ_2. In general, however, the damping ratios (ζ_1 and ζ_2) have less important effects on the system behavior as compared to other parameters. Therefore, priorities should be given to other parameters to tune and optimize the system.

3.3 Investigation on Energy-Harvesting Performance. Again, without loss of generality, we use a three-cell system hereinafter for case studies. The energy-harvesting performance is evaluated using Eqs. (20) and (21).

3.3.1 Effects of k_e on Energy-Harvesting Performance. For the sake of completeness, the electromechanical coupling effect on energy-harvesting performance is briefly discussed. According to the definition of k_e [23] whose physical interpretation is the ability of piezoelectric materials to convert mechanical energy into electrical energy and vice versa, it can be easily inferred that the energy-harvesting performance is closely related to k_e. Detailed studies in the literature [24,25] have shown that in the weak coupling domain, with the increase of k_e, the power can be increased drastically. While, in the strong coupling domain, the maximum achievable power will be saturated, i.e., the increase of k_e cannot guarantee the increase of power. In the following parametric studies, a weak coupling $k_e = 0.02$ is selected because under strong coupling conditions, one peak in the power response will split up into two, and peaks will be flattened, making the power response pattern less recognizable. In addition, for simplicity, each resistor R connected to one transducer is changed simultaneously with the same value all the time, and the power outputs from the resistors are summed up to evaluate the energy-harvesting performance.

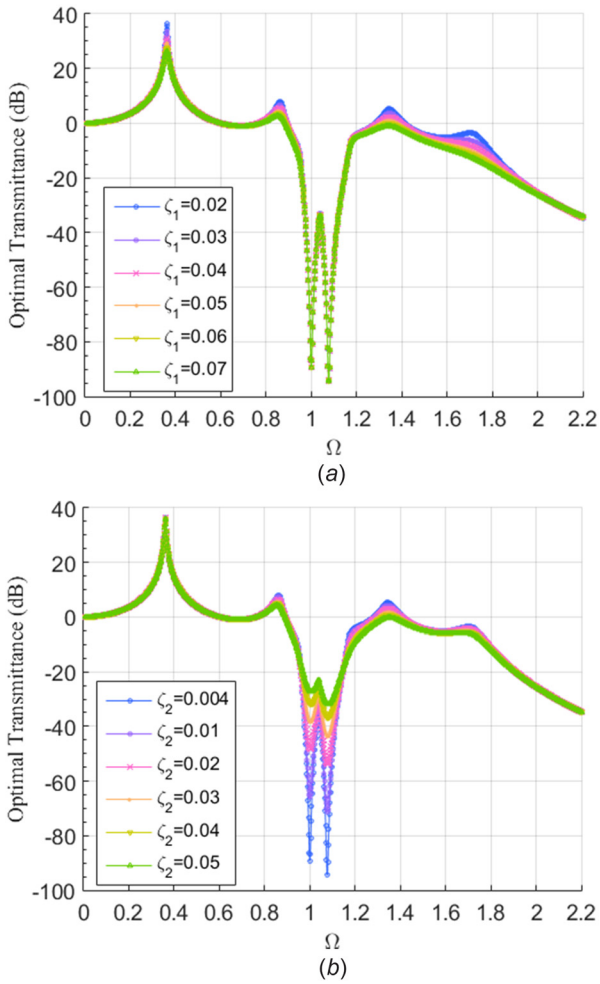

Fig. 8 Optimal transmittance versus Ω for (*a*) different ζ_1 ($\zeta_2 = 0.004$) and (*b*) different ζ_2 ($\zeta_1 = 0.02$)

3.3.2 Effects of μ on Energy-Harvesting Performance. First of all, the effect of μ is investigated. For $\alpha = 0.9;$ $\zeta_1 = 0.02;$ and $\zeta_2 = 0.004$, Fig. 9(*a*) depicts the dimensionless power variation in response to μ. We note that only the magnitude of the first peak is insensitive to μ. Magnitudes of other peaks are sensitive to μ and decrease with it. In addition, the magnitudes of peaks closer to the band gap (refer to Fig. 7(*a*) to check the location of band gap) are more sensitive to μ. Apart from the effect on the magnitudes of peaks, it is also worth noting that the peaks get clustered with a smaller μ. This means that the decrease of μ can achieve not only enlarged but also clustered peaks in the

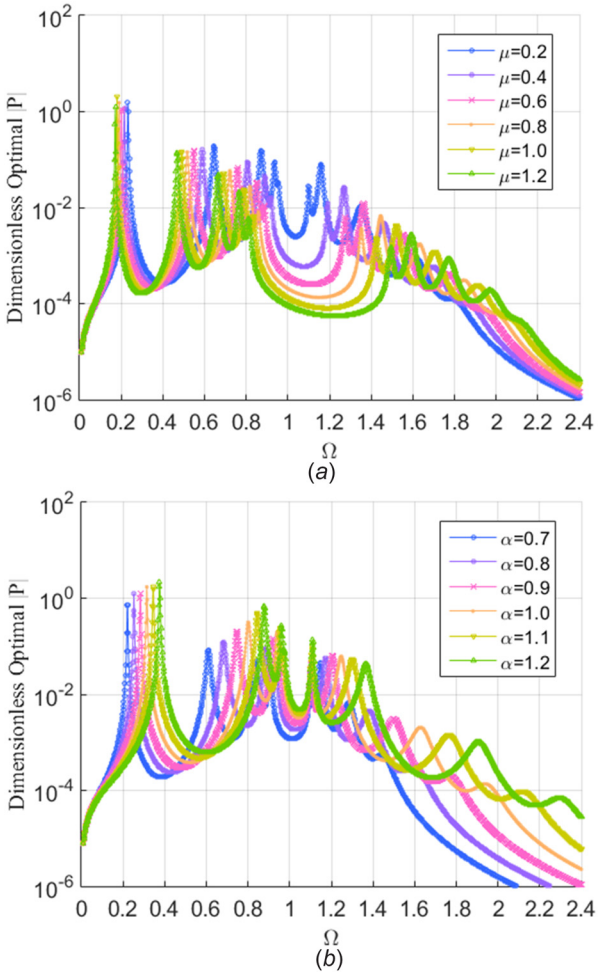

Fig. 9 Dimensionless optimal power versus Ω for (*a*) different μ and (*b*) different α

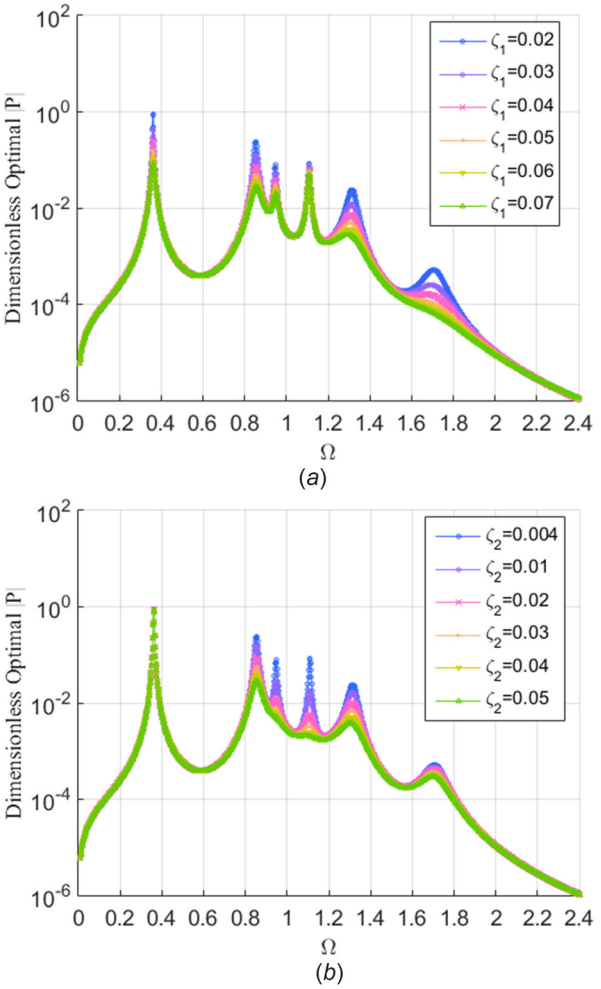

Fig. 10 Dimensionless optimal power versus Ω for (*a*) different ζ_1 ($\zeta_2 = 0.004$) and (*b*) different ζ_2 ($\zeta_1 = 0.02$)

dimensionless power response, which will benefit energy harvesting. This conclusion applies for all the *n*-cell system.

3.3.3 Effects of α on Energy-Harvesting Performance. To investigate the effect of α, we fix $\mu = 0.2; \zeta_1 = 0.02;$ and $\zeta_2 = 0.004$. Figure 9(*b*) shows the dimensionless power with the varying α. It is noted that the peaks shift to the right with the increase of α. This shift is less significant for the peaks near the band gap (refer to Fig. 7(*b*) to check the location of band gap). In addition, the magnitudes of the first four peaks increase, while the magnitudes of the last two peaks decrease with the increase of α. As the magnitudes of the last two peaks are much smaller than the first four, with a larger α, the overall energy-harvesting performance can be improved, even though the last two peaks will be suppressed and drift apart.

3.3.4 Effects of ζ on Energy-Harvesting Performance. For the effect of damping, we assume $\mu = 0.2$ and $\alpha = 0.9$. The effects of ζ_1 and ζ_2 on the energy-harvesting performance are illustrated in Fig. 10(*a*) ($\zeta_2 = 0.004$) and Fig. 10(*b*) ($\zeta_1 = 0.02$), respectively. As shown in Fig. 10(*a*), the magnitudes of all the peaks in the power response decrease with the increase of ζ_1, and the peaks on both sides are more sensitive to ζ_1 than the two peaks in the middle. While from Fig. 10(*b*), an opposite effect is observed for ζ_2. The peaks on both sides are insensitive to ζ_2 while those middle ones are much more sensitive to ζ_2 and decrease significantly with the increase of ζ_2. According to these results, it is concluded that the damping, no matter ζ_1 or ζ_2, should be reduced as much as possible to improve the energy-harvesting performance.

3.4 Impedance Matching Requirements Comparison. In Secs. 3.2 and 3.3, impedance matching was achieved at each frequency for improving vibration suppression performance and energy-harvesting performance, respectively. A question arising spontaneously is that: Are their impedance matching requirements the same? To answer this question, an example with $n = 3$, $\mu = 0.2$, $\alpha = 0.9$, $\zeta_1 = 0.02$, and $\zeta_2 = 0.004$ is given. At each frequency, *r* is swept first to achieve minimal transmittance, then to achieve maximal dimensionless power magnitude. Optimal *r* catering to two different optimization objectives versus Ω for weak coupling ($k_e = 0.02$) and strong coupling ($k_e = 0.4$) is plotted in Figs. 11(*a*) and 11(*b*), respectively. It is found that for most of the excitation frequencies, impedance matching requirements for optimal vibration suppression purpose and optimal energy-harvesting purpose are quite different.

To further investigate the sensitivity of the vibration suppression performance and the energy-harvesting performance to the degree of impedance matching, the transmittance and the dimensionless power responses of the system at two impedance matching schemes (i.e., one scheme for optimal vibration suppression $r_{\text{optimal\_suppression}}$ and the other for optimal energy harvesting $r_{\text{optimal\_power}}$) are shown in Fig. 12.

For weak coupling, Fig. 12(*a*) ($k_e = 0.02$) compares the vibration suppression performance with two impedance cases: (1) the matched impedance $r_{\text{optimal\_suppression}}$ (solid line) and (2) the mismatched impedance $r_{\text{optimal\_power}}$ (dotted line). Similarly, Fig. 12(*b*) compares the energy-harvesting performances with $r_{\text{optimal\_suppression}}$ and $r_{\text{optimal\_power}}$. It is noted that for weak

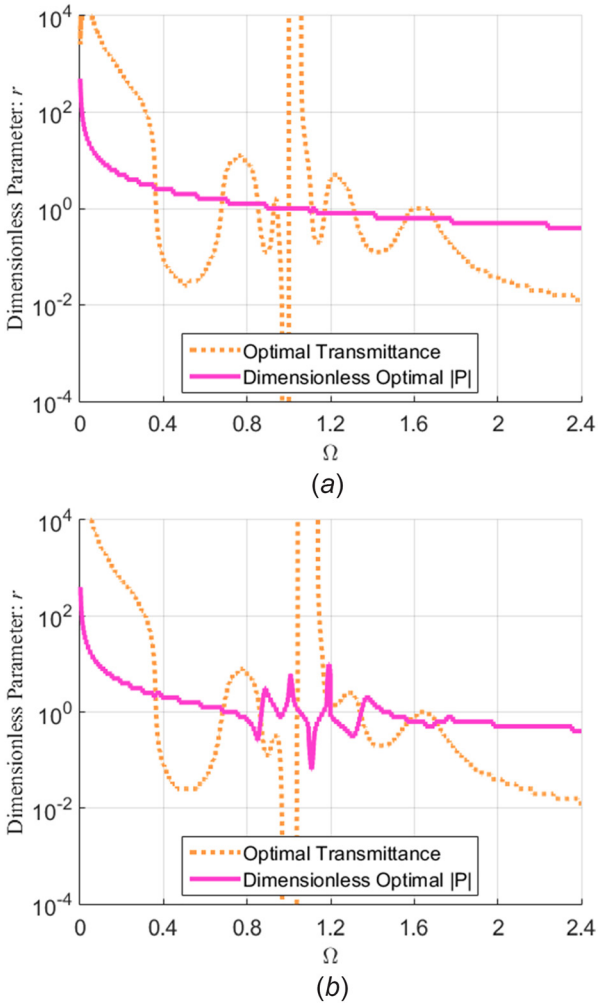

Fig. 11 Comparison of optimal r catering to energy harvesting and vibration suppression, respectively: (*a*) $k_e = 0.02$ and (*b*) $k_e = 0.4$

coupling, the vibration suppression performance of the system is not deteriorated even with mismatched resistive impedance (the transmittance patterns coincided in Fig. 12(*a*)). A physical interpretation is that the weak electromechanical coupling effect on the dynamics of the structure is negligible, and thus, the vibration suppression performance is insensitive to the resistive load. In terms of energy harvesting (Fig. 12(*b*)), it can be observed that power magnitudes at resonant frequencies (i.e., magnitudes of peaks) are almost the same. While farther away from resonant frequencies, power magnitudes corresponding to the impedance matching scheme $r_{\text{optimal\_power}}$ become much higher than the mismatched impedance $r_{\text{optimal\_suppression}}$. This indicates that the impedance matching requirements for two objectives are almost the same in the vicinity of peaks (i.e., for resonance cases), which is implied by those intersection points in Fig. 11(*a*), but become quite different for off-resonance cases. Therefore, we can conclude that for weak coupling condition, attentions and efforts can be paid to improving energy-harvesting performance, with no concern about deteriorating the vibration suppression performance. In other words, for weak coupling, the optimal energy-harvesting performance and quasi-optimal vibration suppression performance can be simultaneously achieved by adopting the scheme for optimal energy-harvesting $r_{\text{optimal\_power}}$.

For strong coupling $k_e = 0.4$, the band gap patterns and dimensionless power responses are shown in Figs. 12(*c*) and 12(*d*), respectively. Different from the weak coupling case, the vibration suppression performance of the system is sensitive to the resistive

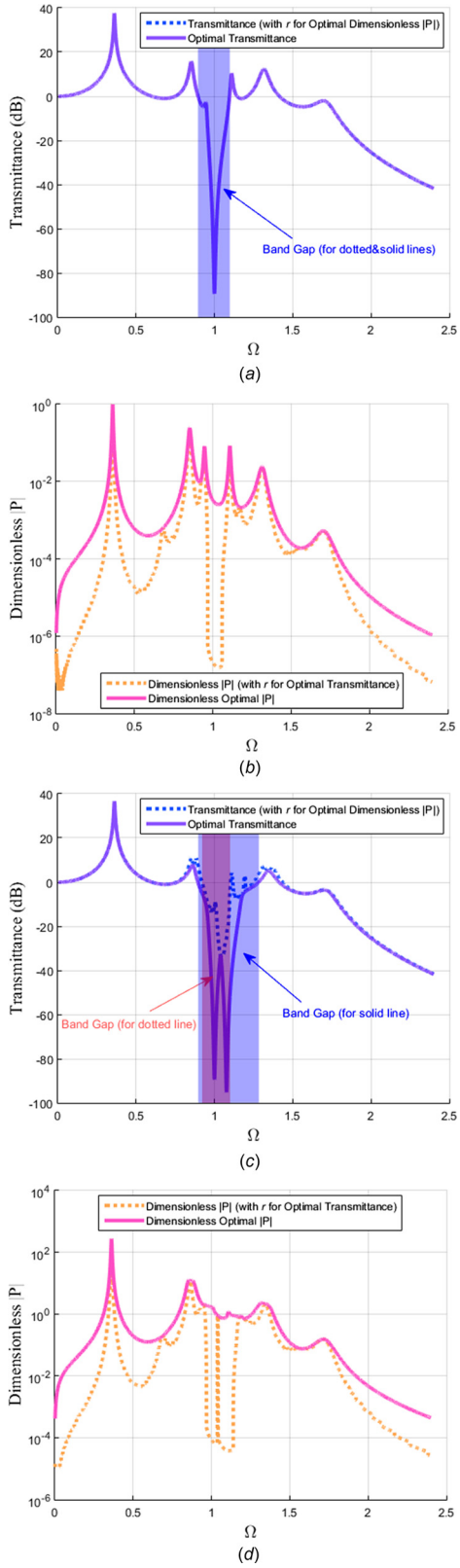

Fig. 12 (*a*) Band gap pattern ($k_e = 0.02$), (*b*) dimensionless optimal power response ($k_e = 0.02$), (*c*) band gap pattern ($k_e = 0.4$), and (*d*) dimensionless optimal power response ($k_e = 0.4$)

impedance and can be enhanced by always tuning an optimal load resistance. This is due to the fact that the additional damping and stiffness induced by the strong coupling become significant and vary with different resistive loads. However, the dimensionless

Table 1 Summary of characteristics of unit-cell and multicell systems

	Vibration suppression		Energy harvesting	
	Unit-cell	Multicell	Unit-cell	Multicell
k_e	With the increase of k_e : More evident double-valley phenomenon Band gap wider Second valley deeper Magnitudes of peaks in transmittance decrease	With the increase of k_e : Peaks near the band gap and peaks in the high-frequency range can be significantly suppressed (the latter is replaced with the second valley)	In the weak coupling domain, the power increases with k_e drastically. While in the strong coupling domain, the maximum achievable power will be saturated	Similar to the unit-cell case
	Preference: larger k_e		Preference: larger k_e	
μ	A larger μ ensures a wider and deeper band gap Though relationship between magnitudes of peaks and μ is not monotonous, a wider gap is more important for vibration suppression	A larger μ ensures a wider and deeper band gap Magnitudes of peaks in the low/high-frequency range increase/decrease with μ. The nearer/farther away to the band gap, the more evident increase/decrease	Two resonant peaks can be tuned closer to each other with a smaller μ	The nearer to the band gap, the more clustered peaks and more significant increase in their magnitudes with a smaller μ
	Preference: larger μ		Preference: smaller μ	
α	With the increase of α : The magnitude of the first peak decreases, while the magnitude of the second peak increases The band gap narrower The valley(s) shallower	The magnitudes of peaks on the left-hand side of the band gap decrease and those on the right-hand side increases with the increase of α The effect of α on magnitudes of peaks weakens for peaks far away from the band gap	The magnitude of the first peak increases with the increase of α, while the magnitude of the second peak is insensitive to α The distance between two resonant peaks is tuneable and can be minimized by adjusting α	With the increase of α : Peaks shifts to the right. This is not significant for the middle peaks close to band gap The magnitudes of peaks on the left-hand side of band gap increase and those on the right-hand side decrease
	Preference: smaller α		Preference: larger α[a]	
ζ_1	Magnitudes of both peaks decrease with ζ_1, and the first peak is more sensitive to ζ_1 Few effects on band gap	Similar to unit-cell system, an additional feature is that the peaks in the middle are less sensitive to ζ_1	Smaller ζ_1 and ζ_2 are always preferred for larger power output	Similar to unit-cell system; an additional feature is that the peaks in the middle are less sensitive to ζ_1
ζ_2	Magnitudes of both peaks decrease with ζ_2, and the second peak is more sensitive to ζ_2 Shallower valleys with the increase of ζ_2	Similar to unit-cell system, an additional feature is that the peaks in the middle are more sensitive to ζ_2		Similar to unit-cell system; an additional feature is that the peaks in the middle are more sensitive to ζ_2
	Preference: larger ζ_1 ; smaller ζ_2		Preference: smaller ζ_1 ; smaller ζ_2	

[a]The peaks on the right-hand side of band gap are insignificant and have minor contribution to energy harvesting.

power response behavior is similar to that under the weak coupling condition—the extracted energy at off-resonant frequencies can be increased if $r_{\text{optimal\_power}}$ scheme is achieved. In virtue of the tacit agreement between impedance matching requirements of two schemes at resonant frequencies (i.e., intersection points in Fig. 11(*b*)), even if we choose the scheme for optimal vibration suppression $r_{\text{optimal\_suppression}}$, the energy-harvesting performance will not be strongly degraded around resonant peaks. Considering the fact that the power extracted in off-resonance conditions is too small for practical use, and the overall energy-harvesting performance is dominated by the power around resonant peaks, the impedance matching scheme for optimal vibration suppression $r_{\text{optimal\_suppression}}$ is thus recommended for strongly coupled system.

4 Summary of Characteristics

In Secs. 2 and 3, we have first investigated a unit-cell system on its vibration suppression performance and then extended our study to a multicell system in terms of its performance of both vibration suppression and energy harvesting. Their characteristics are summarized in Table 1 to give a clear overview, leading to several design guidelines. It is worth mentioning that the conclusions of the characteristics of the energy-harvesting performance of the unit-cell system are profited from the work of Tang and Yang [21].

According to Table 1, we can note that the vibration suppression performance and energy-harvesting performance are almost two contradictory targets. Larger μ and ζ_1 and smaller α are recommended for better vibration suppression performance, while smaller μ and ζ_1 and larger α are preferred for better energy-harvesting performance. Some compromise is indispensable if dual functionalities are demanded. However, we note that larger k_e and smaller ζ_2 are always preferred for both objectives.

5 Conclusion

This paper proposes and analyses a multifunctional AEMM system with piezoelectric elements. A double-valley phenomenon appears in the band gap pattern due to the electromechanical coupling effect that gives rise to the variation of stiffness for the inner system and thus alters its local resonant frequency. The band gap becomes wider for strong coupling condition because of the

existence of the double-valley phenomenon, which indicates that the integration of piezoelectric elements can enhance the original vibration suppression ability of AEMM. Additionally, dimensionless parametric study reveals that by tuning the system parameters μ, α, ζ_1 and ζ_2, the vibration suppression performance can be further enhanced in terms of wider band gap, deeper valleys, and suppressed peaks.

Other than the vibration suppression performance, the energy-harvesting performance is also investigated through a similar dimensionless parametric study. The results show that the system can also be tuned to achieve clustered and enhanced peaks in power response. However, the optimization processes toward dual functionalities demand not only different parameter tuning directions but also different impedance matching requirements. According to the analysis, for a given structure with fixed system parameters, the situation is not so pessimistic. In the weak coupling domain, one can focus on improving the energy-harvesting performance (i.e., the scheme for optimal energy harvesting is recommended) without any concern about deteriorating the vibration suppression performance; whereas in the strong coupling domain, it is suggested to prioritize the vibration suppression performance (i.e., the scheme for optimal vibration suppression is recommended) as energy-harvesting performance will not be remarkably degraded in the vicinity of resonant peaks. Unfortunately, in terms of determining the optimal system parameters, except that larger k_e and smaller ζ_2 are always preferred in the dual-objective optimization process, the contradictions in tuning several other system parameters cannot be eliminated or harmonized: to improve the vibration suppression performance, larger μ and ζ_1, and smaller α are required, while, to enhance the energy-harvesting performance, these three parameters are required to be tuned in the opposite direction.

Acknowledgment

This work was financially supported by the Energy Education Trust of New Zealand (No. 3708242) and the Ph.D. scholarship from the China Scholarship Council (No. 201608250001).

References

[1] Shalaev, V. M., Cai, W., Chettiar, U. K., Yuan, H.-K., Sarychev, A. K., Drachev, V. P., and Kildishev, A. V., 2005, "Negative Index of Refraction in Optical Metamaterials," Opt. Lett., **30**(24), pp. 3356–3358.
[2] Yao, J., Liu, Z., Liu, Y., Wang, Y., Sun, C., Bartal, G., Stacy, A. M., and Zhang, X., 2008, "Optical Negative Refraction in Bulk Metamaterials of Nanowires," Science, **321**(5891), pp. 930–930.
[3] Huang, H. H., and Sun, C. T., 2012, "Anomalous Wave Propagation in a One-Dimensional Acoustic Metamaterial Having Simultaneously Negative Mass Density and Young's Modulus," J. Acoust. Soc. Am., **132**(4), pp. 2887–2895.
[4] Liu, X. N., Hu, G. K., Huang, G. L., and Sun, C. T., 2011 "An Elastic Metamaterial With Simultaneously Negative Mass Density and Bulk Modulus," Appl. Phys. Lett., **98**(25), p. 251907.
[5] Yao, S. S., Zhou, X. M., and Hu, G. K., 2008, "Experimental Study on Negative Effective Mass in a 1D Mass-Spring System," New J. Phys., **10**(4), p. 043020.
[6] Huang, H. H., Sun, C. T., and Huang, G. L., 2009, "On the Negative Effective Mass Density in Acoustic Metamaterials," Int. J. Eng. Sci., **47**(4), pp. 610–617.
[7] Zhu, R., Liu, X., Hu, G., Sun, C., and Huang, G., 2014, "A Chiral Elastic Metamaterial Beam for Broadband Vibration Suppression," J. Sound Vib., **333**(10), pp. 2759–2773.
[8] Ho, K. M., Yang, Z., Zhang, X., and Sheng, P., 2005, "Measurements of Sound Transmission Through Panels of Locally Resonant Materials Between Impedance Tubes," Appl. Acoust., **66**(7), pp. 751–765.
[9] Oudich, M., Assouar, M. B., and Hou, Z. L., 2010, "Propagation of Acoustic Waves and Waveguiding in a Two-Dimensional Locally Resonant Phononic Crystal Plate," Appl. Phys. Lett., **97**(19), p. 193503.
[10] Huang, G. L., and Sun, C. T., 2010, "Band Gaps in a Multiresonator Acoustic Metamaterial," ASME J. Vib. Acoust., **132**(3), p. 031003.
[11] Tan, K. T., Huang, H. H., and Sun, C. T., 2012, "Optimizing the Band Gap of Effective Mass Negativity in Acoustic Metamaterials," Appl. Phys. Lett., **101**(24), p. 241902.
[12] Liu, Y., Sun, X. Z., Jiang, W. Z., and Gu, Y., 2014, "Tuning of Bandgap Structures in Three-Dimensional Kagome-Sphere Lattice," ASME J. Vib. Acoust., **136**(2), p. 021016.
[13] Chen, Y., Huang, G., and Sun, C., 2014, "Band Gap Control in an Active Elastic Metamaterial With Negative Capacitance Piezoelectric Shunting," ASME J. Vib. Acoust., **136**(6), p. 061008.
[14] Chen, Z. S., Guo, B., Yang, Y. M., and Cheng, C. C., 2014, "Metamaterials-Based Enhanced Energy Harvesting: A Review," Phys. B Condens. Matter, **438**, pp. 1–8.
[15] Carrara, M., Cacan, M. R., Toussaint, J., Leamy, M. J., Ruzzene, M., and Erturk, A., 2013, "Metamaterial-Inspired Structures and Concepts for Elastoacoustic Wave Energy Harvesting," Smart Mater. Struct., **22**(6), p. 065004.
[16] Shen, L., Wu, J. H., Zhang, S. W., Liu, Z. Y., and Li, J., 2015, "Low-Frequency Vibration Energy Harvesting Using a Locally Resonant Phononic Crystal Plate With Spiral Beams," Modern Phys. Lett. B, **29**(1), p. 1450259.
[17] Mikoshiba, K., Manimala, J. M., and Sun, C. T., 2013, "Energy Harvesting Using an Array of Multifunctional Resonators," J. Intell. Mater. Syst. Struct., **24**(2), pp. 168–179.
[18] Ahmed, R. U., Adiba, A., and Banerjee, S., 2015, "Energy Scavenging From Acousto-Elastic Metamaterial Using Local Resonance Phenomenon," Proc. SPIE, **9431**, p. 943106.
[19] Huang, H. H., and Sun, C. T., 2011, "Locally Resonant Acoustic Metamaterials With 2D Anisotropic Effective Mass Density," Philos. Mag., **91**(6), pp. 981–996.
[20] Khelif, A., and Adibi, A., 2015, *Phononic Crystals: Fundamentals and Applications*, Springer, New York.
[21] Tang, L. H., and Yang, Y. W., 2012, "A Multiple-Degree-of-Freedom Piezoelectric Energy Harvesting Model," J. Intell. Mater. Syst. Struct., **23**(14), pp. 1631–1647.
[22] Kim, H., Priya, S., Stephanou, H., and Uchino, K., 2007, "Consideration of Impedance Matching Techniques for Efficient Piezoelectric Energy Harvesting," IEEE Trans. Ultrason. Ferroelectr. Freq. Control, **54**(9), pp. 1851–1859.
[23] Moheimani, S. R., and Fleming, A. J., 2006, *Piezoelectric Transducers for Vibration Control and Damping*, Springer Science & Business Media, New York.
[24] Lefeuvre, E., Badel, A., Richard, C., and Guyomar, D., 2005, "Piezoelectric Energy Harvesting Device Optimization by Synchronous Electric Charge Extraction," J. Intell. Mater. Syst. Struct., **16**(10), pp. 865–876.
[25] Guyomar, D., Badel, A., Lefeuvre, E., and Richard, C., 2005, "Toward Energy Harvesting Using Active Materials and Conversion Improvement by Nonlinear Processing," IEEE Trans. Ultrason. Ferroelectr. Freq. Control, **52**(4), pp. 584–595.